ADVANCED FUNCTIONAL MATERIALS
www.afm-journal.de

Electronic Instabilities Leading to Electroformation of Binary Metal Oxide-based Resistive Switches

Abhishek A. Sharma, Mohammad Noman, Mohamed Abdelmoula, Marek Skowronski, and James A. Bain**

Oxide-based resistive switching devices are a leading contender for the next generation memories. Before use, each device has to go through a conditioning process called electroformation which has been suggested to be initiated by the accumulation of oxygen vacancies. Here, experimental evidence is presented which shows that both Ta_2O_{5-x}- and TiO_{2-x}-based crossbar devices, exhibit characteristic electronic instability leading to a reversible constriction of the current flow to a narrow filament prior to permanent change. Thus, it is asserted, electroformation is initiated through purely electronic and reversible events, to be followed later by structural changes in the material, like oxygen vacancy redistribution. Furthermore, the electronic instability responsible for electroformation also gives rise to negative differential resistance (NDR) and that this characteristics appears to involve two distinct mechanisms: a thermal one in which Joule heating causes resistance to decrease as current increases and a second electronic mechanism that appears not to require Joule heating for NDR. Using a combination of thermometry and thermal modeling, a self-consistent temperature and filament radius as a function of power are found for the 5 μm cross-bar devices. In the thermal NDR regime, the filament appears to be ~500 nm in diameter and has a peak temperature of ~300 °C, while in the adiabatic regime, the estimated filament diameter is much smaller (<50 nm) and the maximum temperature inside it exceeds 800 °C.

1. Introduction

In its 50 year long history, resistive switching phenomena have been subject to increasing levels of scientific and technological scrutiny as potential candidate for non-volatile memory. The most important factors that make oxide-based resistive memories technologically viable are scalability, simplicity of structure, and use of traditional foundry materials. The scalability argument relies on the now accepted mechanism of nano-scale conductive filaments that participate in switching. These filaments disconnect and re-form causing the device to show distinct high and low resistance states. The two resistance states are then utilized as the states of the memory.[1–10]

The permanent filaments are typically thought of as an oxygen deficient cylinder with oxygen vacancies that are either distributed randomly or form a metallic secondary phase, such as the Magneli phases in TiO_2.[11] In most cases, the filaments have to be induced in the functional layer using a one-time programming process known as 'electroforming' (or simply 'forming') which typically is accomplished by application of a quasi-DC voltage sweep. At some point during the sweep and at a voltage typically exceeding the switching voltage, the device experiences a sudden increase in current. It has been proposed that the increase in current occurs when a structural filament extending from the anode makes a contact with the other electrode.[11] This model, however, has difficulties with interpretation of some transient phenomena observed in switching devices. Ielmini et al.[36] reported a "recovery" event in NiO-based devices. Here, the devices remain unaffected despite undergoing a rapid decrease of resistance due to a forming-like event, and returned to the original state. Also, Noman et al. argued that the current filament forms before permanent changes in the structure of the device take place.[40] Both observations imply that conductance of at least some switching devices increases due to electronic effects rather than defect formation. Of course, atomic migration is ultimately present and manifests itself in the formation of permanent conducting filament, as is common in phase change chalcogenides[12] and polysilicon fuses.[13] The main point of the present work is that electronic process can initiate filamentation in cases where random local defects/non-uniformities do not exist; and can assist in filament nucleation and growth if the random local defects do exist in the material.

A number of authors,[14–19,37–40] notably among them Alexandrov et al., have realized the inherent difficulty in forming the permanent filament and implied the existence of an electronic effect in the form of a "soft breakdown". Some authors have suggested that instability in oxides could be similar to threshold switching observed in chalcogenides.[26–29,36] However, such studies have, not presented a direct and comprehensive evidence of electronic filamentation. Moreover, the origins

A. A. Sharma, Dr. M. Noman, Prof. J. A. Bain
Electrical & Computer Engineering Department
Carnegie Mellon University
5000 Forbes Ave.
Pittsburgh, PA 15213, USA
E-mail: abhisheksharma@cmu.edu; jbain@ece.cmu.edu
Dr. M. Abdelmoula, Prof. M. Skowronski
Materials Science & Engineering Department
Carnegie Mellon University
5000 Forbes Ave.
Pittsburgh, PA 15213, USA

DOI: 10.1002/adfm.201400461

of the instability i.e. whether the instability is due to localized lattice heating or hot electrons effects remain unknown. Here, we present unambiguous evidence, for TiO_{2-x} and Ta_2O_{5-x}, that an initially uniform current flow can spontaneously and reversibly constrict to a localized filament of increased current density, without structural change. Furthermore, our examination reveals a two-step process of current localization, with the event being initiated by a gradual thermally-mediated process, followed by a more rapid electronic process.

2. DC Forming

Figure 1 shows two quasi-DC *I–V* characteristics obtained from a single crossbar-type $Pt/Ta_2O_5/Pt$ device. The two curves were obtained using different values of series resistor, R_s (the circuit schematic is shown in Figure 1(b)). The measurements were made by sweeping the source voltage while measuring the voltage across the device (V_m in the figure). Adding the series resistance in the circuit implies that a higher voltage from the source is needed to reach the same *I–V* point of the device (slope of the load-line i.e. $-1/R_S$ is shallower for high R_S). A voltage ramp rate of 4 V/s has been used for the experiment for the generated curves (slower ramp rates did not change the behavior of the cells). The black line marks the *I–V* obtained with R_S = 100 Ω. Starting at low voltages, the curve increases super-linearly and then at 5.75 V snaps back (electroforms) leaving the device in the low resistance ON state. The decrease of resistance is permanent although the device can be switched between ON and OFF states repeatedly. The current value after the snap-back for the R_S = 100 Ω case, reaches about 180 μA due to the current compliance (with a likely overshoot during snap-back). The electroformation event is effectively instantaneous on the time scale of the source meter response with no intermediate states recorded. The red *I–V* curve which was collected beforehand, does not show a permanent change and can be retraced for decreasing source voltage. The red curve corresponds to R_S = 34 kΩ (standard ohmic resistors of 33.7 kΩ

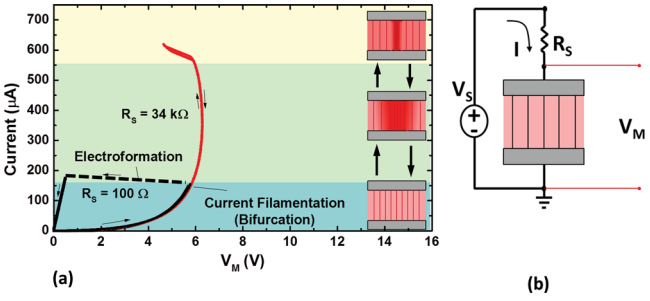

Figure 1. Observation of negative differential resistance (NDR) in Ta_2O_{5-x}. (a) Electroformation with a 'snap' observed in samples with 100 Ω series resistance (black trace). This is prevented by using a large source resistance (red trace). Stable and reversible current filamentation causes the device *I–V* to show negative differential resistance (NDR), post-bifurcation. The three color-zones indicate uniform conduction (blue), thermal filamentation (green) and filament collapse (yellow). Inset on the right shows a schematic of the change in conducting area as the device is driven to filamentation, but should be taken as only semi-quantitative. (b) Circuit schematic shows the experimental setup with V_M representing the device voltage.

chosen for experimental convenience; 300 Ω was added due to the resistance of pad and cross-bar traces). At low voltages, it follows the same path as the one for R_S = 100 Ω but extends to higher current values without forming. At about 6 V, the *I–V* trace gradually bends back forming a part of an S-type curve characteristic of current-controlled negative differential resistance (CC-NDR). The presence of CC-NDR usually indicates the presence of an instability that can lead to the spontaneous formation of localized high current density filaments within the device.[24] This phenomenon is characteristic of nonlinear dynamic systems and is often referred to as bifurcation. This also implies that the system will 'snap' to a low resistance state (in this case, the current runaway will result in permanent change of resistance i.e. forming) whenever the total differential resistance becomes negative (dV_S/dI in (2). To define the total differential resistance, we first break the source voltage, V_S, into the voltage drop across the device, V_D, and the voltage drop across the series resistor, V_{RS}:

$$V_s = V_D + V_{Rs} \tag{1}$$

The total differential resistance, dV_S/dI, (where I is the series current flowing through both devices) is then given by:

$$\frac{dV_s}{dI} = \frac{dV_D}{dI} + \frac{dV_{Rs}}{dI} \tag{2}$$

By increasing the source resistance (R_S), one can limit the range of voltages corresponding to negative total differential resistance (dV_S/dI) and increase the range accessible to testing. This enables the device to support a stable filament and a corresponding negative differential device resistance (i.e. dV_D/dI negative). At sufficiently large RS, the total differential resistance becomes positive (due to dV_{RS}/dI positive) and the snap-back associated with runaway can be prevented altogether. In other words, if the dV_{RS}/dI is not large enough (due to small R_S), the device will filament instantaneously, as it goes through a snap. The different types of *I–V* in Figure 1 are, therefore, fully consistent with each other and can be explained without invoking any changes of the device structure. In other words, the R_S enables us to stabilize the pre-forming *I–V* by stabilizing the electronic filament and defines the *I–V* path of the device post-bifurcation. This makes the post-bifurcation *I–V* distinct in each case. The insets in Figure 1(a) schematically represent the current constriction process. At low voltages, the differential resistance of the device is positive and the current flow is uniform (bottom schematic). With increase of voltage, the device approaches the NDR region and the current flow constricts to a filament with relatively large diameter (middle schematic). With further increase of source voltage (V_S), the voltage across the device and the diameter of the filament decrease and at the sharp turn of the *I–V* curve collapse to a very small filament. The procedure used to extract the size of the filament from *I–V* curves is described later in the text.

While the data in Figure 1 were obtained on Ta_2O_{5-x}-based devices, we have observed similar behavior in other switching oxides. **Figure 2** and **Figure 3** present the results obtained on $Pt/TiO_2/Pt$ devices. Figure 2(a) shows a typical forming *I–V* with the source resistance of 700 Ω. Initially highly resistive

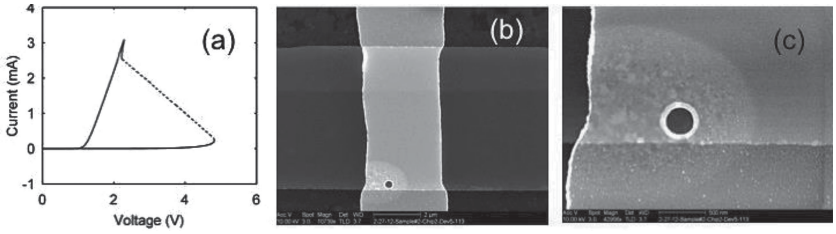

Figure 2. (a) Electroforming *I–V* characteristics of the Pt/TiO_2/Pt 5 μm cross-bar device with the source resistance of 700 Ω. (b) SEM image using through-lens detector of the device after electroforming and (c) a high magnification image of the lower left corner of the same device.

device exhibits forming at 4.7 V with the device formed to high resistance OFF state. The dashed line in the figure corresponds to the load line. The electroformation of TiO_2 devices frequently leads to changes in the top electrode morphology which were observed in scanning electron microscopy (SEM) images. Several groups reported formation of "bubbles" and /or craters forming at the location of the filament and interpreted as due to local heating.[1,11,23,26] The changes in the device shown in (a) were imaged by SEM using a through-the-lens detector (Figure 2(b) and (c)). The low magnification image shows a horizontal stripe corresponding the to bottom electrode and much brighter the vertical top electrode stripe. The most visible feature is the dark dot with a bright edge located in the lower left corner of the active area. The dot is surrounded by a bright "halo". The high magnification image of this feature is shown in Figure 2(c). It is quite apparent that the dark dot corresponds to the area where platinum film delaminated exposing the functional layer underneath. This could be due to either local melting of the metal or solid state diffusion at elevated temperatures. It is widely accepted that such features form at the location of the filament. The "halo" shows a contrast characteristic of polycrystalline grains in a metal. The center portion has grain size of about 100 nm (as measured by an SEM) gradually tapering down to 10 nm toward the edge. We interpret this contrast as the result of Joule heating in a small diameter filament and the resulting grain growth in the Pt electrode. By limiting the current overshoot during electroformation we can eliminate the delamination of Pt but all of out electroformed TiO_2 devices show signs of the halo.

Figure 3 shows the *I–V* characteristics of a similar TiO_2 crossbar obtained with R_S = 4.7 kΩ. The overall I-V shape is similar to that obtained on Ta_2O_{5-x} samples with clear CC-NDR behavior and a distinct change of slope in the upper part of the curve at 2 V. In the later part to this report, we interpret such change as due to two different mechanisms contributing to the increase of conductivity with applied bias, namely thermal and electronic. SEM micrograph in the inset shows the contrast of the top electrode after the test. The contrast across the device is uniform with the exception of a bright circular area with the diameter of about 0.7 μm located near the left edge of the device. The feature has all characteristics of the halo shown in Figure 2 and is consistent with current constriction to a small diameter filament associated with NDR. The above observations indicate that the voltage and temperature non-linearity is characteristic of most resistive switching oxides.

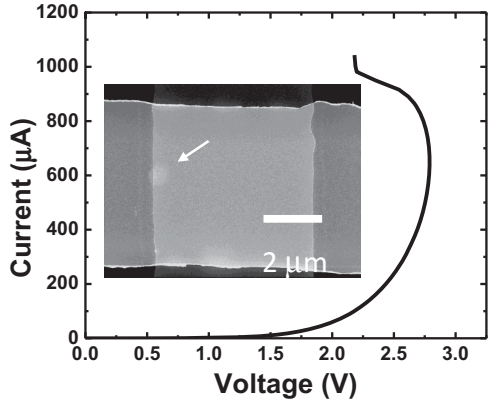

Figure 3. Negative differential resistance observed in 20 nm thick TiO_{2-x} cross-bar with R_S = 700 Ω. SEM image (inset) shows the evidence of the current constriction in the CC-NDR voltage range.

3. Dynamics of Forming

Additional insight into the dynamics of the electroformation process and current filamentation was obtained using time domain transmissometry (TDT) (detailed description in the Supporting Information – S1,S2). It must be noted that TDT is a technique that enables delivery of high-fidelity voltage pulses to the device and reading off the transmitted voltage pulses and current through the device without any parasitic overshoots. For the pulse forming experiment, we use constant voltage pulses applied across the device and a 100 Ω resistance connected in series. TDT allows for monitoring the change of voltage across the device and current as a function of time. Identical devices can be formed at a wide range of voltages, with lower voltages requiring longer incubation time before the device undergoes the electroformation.[25]

Figure 4(a) shows the voltage across the device as a function of time. Each curve corresponds to the trace during a single voltage pulse applied to the same Ta_2O_{5-x} device. Our previous work shows the dependence of electroforming time on forming voltage.[25,41] In experiment described here, each pulse had the same amplitude (one of the voltage conditions observed in our earlier work) but slightly different duration, allowing for the interruption of the process at different stages, a few nanoseconds prior to the completion of forming. As the pulses applied brought about reversible changes (explained below), we were able to use the same device for the entire experiment. The oscilloscope trace started at t = 0 with a fast rise-time of the voltage at the leading edge of the applied pulse (not shown). This was followed by a gradual decrease of voltage (initial negative slope) which is associated with decrease of device resistance due to Joule heating. It must be noted here that, while the device has high resistance (~1 MΩ) at low biases, it shows a low resistance (~5 kΩ) at high biases (~11 V across the device), following a strong voltage non-linearity ($R \propto V^{-2}$), as shown in **Figure 5**(b) and our previous works.[25,40,41] This part of the transient can

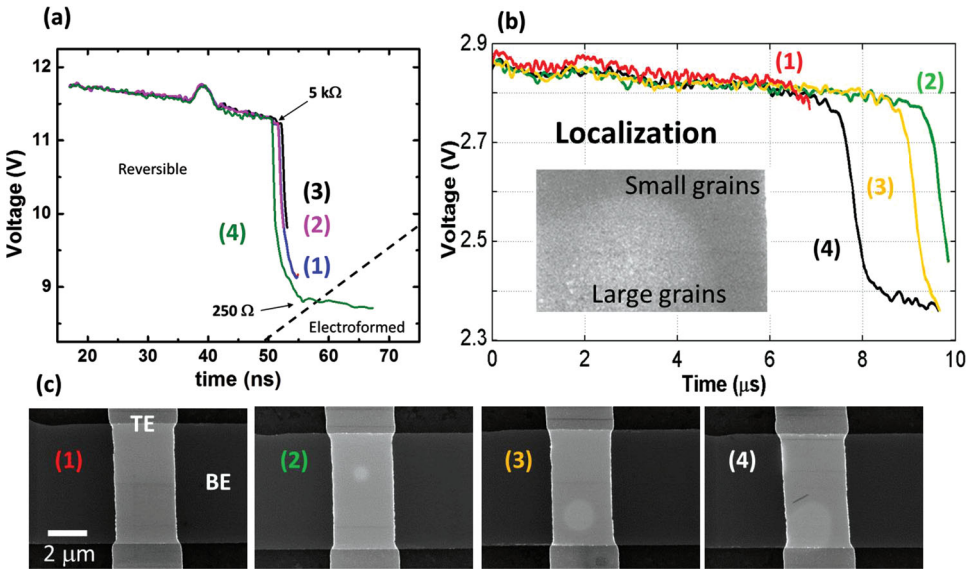

Figure 4. Pulsed electroforming experiments. (a) Voltage dynamics obtained by pulsing the device repeatedly (1 through 4) with different pulse durations for the same Ta_2O_{5-x} device. Large resistance change observed without any permanent change until pulse 4. (b) Similar pulse reversibility experiments on TiO_{2-x} show morphological changes (shown in (c)) due to higher power dissipation compared to Ta_2O_{5-x}.

be accurately simulated using known materials parameters and assuming uniform current flow,[40] [discussed in S2 for Ta_2O_{5-x}]. The bump at 38 ns is due to a parasitic pulse reflection in the system while the rapid drop between 45 and 55 ns corresponds to the beginning of the electroformation process (and we arrest the pulse at different points, in this range). We assert this based on the magnitude of the resistance change of the device. For example, the device resistance during pulse 4 (green curve in Figure 4(a)) at the onset of the rapid drop is 5 kΩ and the resistance value at the point of pulse termination is 250 Ω. This change is too big to be explained by thermal effects in the uniform conduction regime. Moreover, while there was no permanent change of the device resistance after pulses 1–3 terminating before the completion of the process, the device was formed after the pulse 4. The resistance did not recover and remained at the 250 Ω level after the pulse. The conclusion here is that the rapid drop in resistance in Figure 4(a) does correspond to the electroformation process. The initial part of the sharp reduction of resistance is volatile and therefore has to be electronic in nature rather than one involving atomic motion.

The results of the similar experiment performed on TiO_{2-x} devices are presented in Figure 4(b). Each voltage transient and the corresponding SEM image were collected on a different but nominally identical device and each device was exposed to only one pulse. Different devices were used in this experiment for the ease of SEM imaging, while making sure that the incubation time before resistance change (reversible forming, akin to Ta_2O_{5-x}) is the same for all the devices under test. The images show the cross bar-type devices with the light grey vertical strip corresponding to the top electrode and the horizontal darker grey strip corresponding to the bottom electrode. The active area of the devices is the rectangle at the intersection of the electrodes. As in Figure 4(a), the pulses were interrupted at various stages of the electroformation process. Traces 1–3 correspond to devices that retained their original resistance after the pulse while trace 4 corresponds to the device on which the electroformation was completed with the permanent drop of resistance. The red trace (1) corresponds to the process interrupted during the uniform current flow stage. The SEM image obtained after this single pulse shows perfectly uniform contrast over the active part of the device. SEM image obtained on the device which experienced the first part of rapid decrease of voltage (trace 2 in Figure 4(b) and image 2 in (c)) shows a characteristic halo with diameter of 1.5 μm. The size of the halo on the device which experienced larger resistance decrease (trace 3) increased to 2 μm eventually attaining diameter of 3 μm on the device with permanent resistance change. Such morphological changes on the top electrode are not seen on Ta_2O_{5-x} devices apparently as a result of lower temperature excursions. This observation is a direct evidence of current filamentation occurring before any permanent changes (such as vacancy accumulation) take place in the memristive devices. This instability is reversible and electronic in nature. Only at its later stages and after the core of the filament reaches high temperatures due to high current density, do the physical changes in the device structure take place. The behavior described above is somewhat similar to the transient threshold switching reported in chalcogenides.[12] Whether the NDR-type characteristics are purely a result of heating or supplemented by field dependent conductivity is assessed in the following sections.

4. Temperature Dependent Onset of Filamentation

In this section, we will try to experimentally assess the role of Joule heating in NDR and filament formation. Figure 5(a) shows three I–V characteristics: the black and red traces are DC I–V with R_S = 100 Ω and 34 kΩ, respectively, as shown in Figure 1(a). Since the sweep rate is low, the devices reached thermal steady state at every point (i.e. they heated up). The

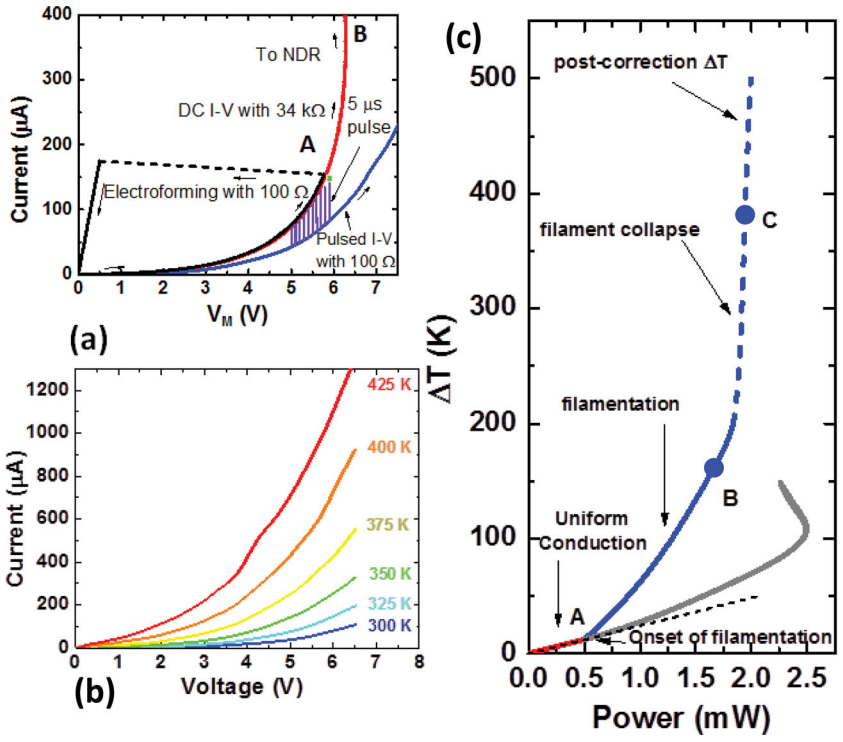

Figure 5. Temperature and voltage non-linearities as the origin of filamentation. (a) Adiabatic pulsed *I–V* shown in blue taken when the device did not undergo any self-heating. The violet *I–V* dynamic curves connect the initial and the final I vs. T and V vs. T points at 1 ns and 5 μs. Electroformation occurs in the 5 μs long pulses at the same V, I combination (green spot) as the DC case (black). (b) Adiabatic pulsed *I–V* curve taken as a function of temperature displaying non-linearities in both temperature and voltage. (c) ΔT vs. P obtained by applying thermometry to the DC *I–V* taken with a 34 kΩ resistor in series (red, gray curve). Blue curve shows the corrected local temperature. Non-uniform conduction sets in at point A due to thermal non-linearity. Region B represents the thermal onset of filamentation followed by a sharp collapse of the filament due to field/current density dependent instability (Region C).

points on the blue curve were obtained in a pulsed experiment where the current and voltage across the device was measured 1 ns after the pulse leading edge. Since the thermal time constant of our devices was experimentally measured in our earlier work[25] to be about 2.5 μs, one can assume that the temperature of the device remained at the stage temperature. It is apparent that excluding the self-heating (blue curve) extended the range of voltages that could be reached without device forming and reduced the current at any given voltage eliminating the CC-NDR. In other words, a device not undergoing self-heating (pulsed *I–V*), would have a much higher breakdown voltage and current compared to ones that undergo DC forming. Next, we try to experimentally establish the relation between the pulsed *I–V* and the DC *I–V*. In addition to three *I–V* curves, Figure 5(a) also shows the results of another series of pulsing experiments represented by almost vertical violet lines. The pulse duration in this experiment was always 5 μs and the violet line corresponds to voltage and current evolution across this 5 μs pulse due to Joule heating. During the pulse, the temperature of the device evolves (also illustrated in our earlier work,[25] approaching the steady state at 5 μs. The coincidence of the end points in this experiment and the black trace (DC with the same load resistor) confirm that filamentation and CC-NDR in the low voltage/current range is purely a thermal phenomenon. In other words NDR appears because the device becomes more conductive as it carries more current because of self-heating creating a positive-feedback. Accordingly, the origin of NDR in this part of the *I–V* characteristics appears to be thermal.

While we have argued that CC-NDR indicates filamentation, it is not clear, at which specific voltage the filament forms or the temperature the local electronic filament reaches before breakdown. We can estimate this by analysis of the dependence of device temperature on dissipated power. For the sake of discussion, let us assume that the current flow is uniform for the entire *I–V* curve obtained with R_S = 34 kΩ (Figure 1(a)). The device temperature at every voltage was extracted from the pulsed *I–V* measurement calibration as a function of stage temperature, shown in Figure 5(b). This data maps the non-linear dependence of current on voltage and temperature and allows the device resistance itself to serve as a thermometer. It should be noted here that the pulsed-*I–V* measurements were extended up to 18 V (not shown here) the maximum range of voltages which do not result in electroformation during 5 ns long pulses.[41] In Figure 5(c), we use this thermometry technique to plot the rise in steady-state temperature due to Joule heating during the DC voltage sweep as a function of power dissipated in the device (red trace). The expected rise in temperature should depend linearly on power:

$$\Delta T = R_{th} P \tag{3}$$

where, ΔT is the rise in temperature in Kelvin, R_{th} is the thermal resistance seen by the source of heat, and P is the power dissipated at the heat source. The thermal resistance, in turn, can be expressed as:

$$R_{th} = \frac{1}{k_{th}} \frac{t}{A} \tag{4}$$

where, k_{th} is the thermal conductivity of the materials leading to the thermal ground, t is the distance the heat travels to thermal ground and A is the area getting heated up (in steady state) and depends on the filament size. At low voltages, the current flow is uniform and A corresponds to the area of the device. This gives the constant slope of 0.025 K/μW in Figure 5(c)). This slope corresponds to an R_{th} which is consistent with the thermal resistance felt by a uniformly conducting 5 μm square device deposited on 1 μm thick SiO_2. At 600 μW, the $\Delta T(P)$ slope increases indicating the onset of current constriction (point A in the DC *I–V* curves). The subsequent section of the curve is gray (at powers above 600 μW) to indicate that

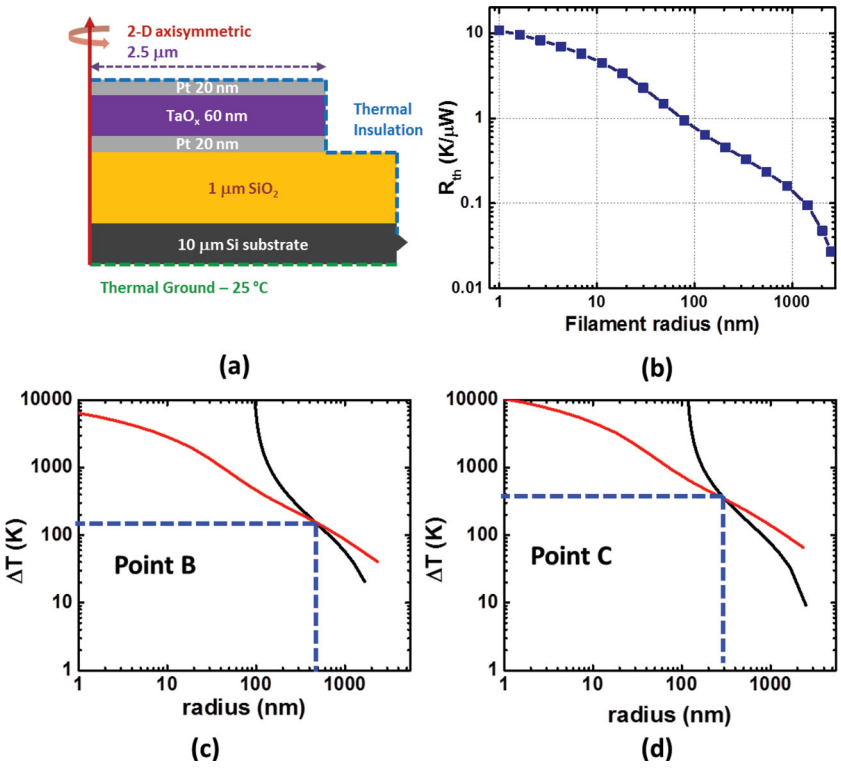

Figure 6. True filament temperature extraction. (a) Schematic of the Ta_2O_{5-x} device used in Comsol Multiphysics electrothermal simulations. (b) Simulated thermal resistance (R_{th}) as a function of filament radius. (c,d) ΔT extracted by parameterizing different radii with (b) – red curve; and using pulsed I–V (black curve) shown at different powers corresponding to points B and C in Figure 5(c).

the temperature calibration is no longer correct when filamentation sets in; the gray section can only be taken to be a lower bound on the device temperature. As the bias increases further past the onset of filamentation, the slope continues to increase indicating gradual reduction of the filament diameter. The deviation from the initial slope up to 2 mW is attributed to thermally induced CC-NDR. Following this, a steep change of slope occurs at higher powers indicating that the mechanism of the non-linearity is completely different from the one that occurs at point A. This region corresponds to the collapse of the filament resulting into a very localized current flow, which we refer to as the electronic filamentation (making a clear distinction in the non-linearities).

After filamentation onset, the temperature reached is a strong function of filament diameter, with greater current localization leading to higher temperature. Rather than simply postulating a filament size and then estimating the temperature based on that assumption, we have attempted to extract a filament size self-consistently from our data by reconciling temperature rise as estimated from thermal modeling and temperature rise estimated from conductivity change. We assume, in this case, that the conduction through the reversible current filament (which is continuous through thickness) dissipates power uniformly through the thickness of the film, unlike switched films, as noted by Menzel et al.[42] At the high temperature regimes that we are operating in, we think that the electrons have sufficient energy to overcome any barrier that may exist between the oxide and Pt electrode. Additionally the very low resistance of the electronic filament suggests that very little interface resistance, which would localize the power drop at one or both electrodes is present. The true temperature is calculated with a self-consistent solution for a filament size under the constraints of simultaneously satisfying the adiabatic I–V–T relationship (Figure 5(b) with extrapolation as necessary) and the R_{th} experienced by the same filament size. The adiabatic I–V–T relationship measured with pulsed I–V technique indicates how much power is generated in the device at a given temperature for a combination of current density, J, assuming a filament size. The R_{th} is a measure of how effective can the generated power be dissipated and is unique to a given filament size. As R_{th} represents the thermal resistance that is connected between the filament as the heat source and the thermal ground, it can be easily calculated from material properties and a steady state finite element simulation. We use Comsol Multiphysics finite element method solver for the calculation of the R_{th} as the ratio of the rise in temperature experienced with unit increase in the power dissipated in the filament, at steady state. **Figure 6**(a) shows the simulation setup used for the solver. The results of the simulation are summarized in Figure 6(b). From this figure, then, it is possible to estimate the temperature given a filament radius and the measured power dissipated in the device after the onset of the filamentation.

We also know that when we estimate ΔT from the pair of I–V coordinates, we assume that the current flows through a filament of radius 2.5 µm, i.e. uniform conduction. Thus, for a device undergoing filamentation, we will always underestimate the local filament temperature. Scaling the current axis in the I–V–T thermometer (Figure 5(b)) by the ratio of the uniform device area (conduction radius r = 2.5 µm) and the filament radius, r we get a new range of temperatures for an effectively higher current density. Thus, the corrected curve so constructed is a SECOND, independent figure we can consult to extract a temperature from an assumed filament radius and known I and V measurements. Figures 6(c) and (d) consist of two curves each. The red curves represent the ΔT obtained by multiplying the power at points B and C in Figure 5(c) with the R_{th} and parameterizing the radius. The black curves represent the temperature rise predicted by the pulsed I–V with parameterized current density for different filament radii. The unique intersection of the two curves is used at each power level to calculate the true filament temperature and radius as the device undergoes electronic constriction of current. Thus, these two constraints are simultaneously applied to the DC measurement to yield the true localized temperature of the device as it undergoes thermal and electronic filamentation. This gives the blue trace (full details of the extraction procedure

are explained in the supplement S3). The solid line represents the extraction of temperature made within the experimental limits of the adiabatic *I–V–T* measurement. The dotted lines indicate the non-linear extrapolation of the measurement data. The non-linear extrapolation was made by assuming a space-charge limited conduction (to which the data matches). It must be noted that the entire NDR curve (up to point C) is reversible and hence we assert the nature of this localization to be electro-thermal and preceding the motion of atoms or vacancies.

Moreover, such deviation is also seen in dynamics measurements in TiO_{2-x},[40] [more details in S2 for Ta_2O_{5-x}]. The device temperature can be both measured and simulated till just prior to resistance drop. Temperature rises ranging from 10–150 K have been measured in devices prior to filamentation in pulse experiments (range refers to the pulse voltage used to form the device, like our previous work.[25]

5. Discussion

We have presented the experimental evidence of electronic instability in oxide materials commonly used in fabrication of memristive devices. During the approach to the instability, the temperature gradually increases linearly with power to about 320 K. At this point the current flow constricts and the actual temperature of the filament increases faster than uniform current flow calibration. For the $Pt/Ta_2O_{5-x}/Pt$ device discussed in this work, the steady temperature reaches ~500 K as the extracted filament diameter reduces from 5 μm (uniform conduction) to 1 μm due to thermal NDR. Additional power produces further filament collapse, and temperature increases rapidly, reasonably estimated as high as 1000 K as the filament diameter collapses to ~10 nm (same as reported by Kwon et al.[11] The filament diameter estimation has been explained in the supplementary document. These temperatures provide sufficient activation energy to change the oxide in the different ways reported in literature – cause oxygen vacancy creation, crystallization, secondary phase formation[27] and/or melting of the top electrode.[11] The proposed mechanism explains these changes and removes the inconsistency in explaining reduction of the oxide at low temperature. It parallels the mechanism that has been widely accepted in chalcogenide glasses and referred to as "threshold switching".[12,26–29]

The CC-NDR in metal/oxide/metal structures have been reported number of times in the literature.[19–22] Most observations have been made on electroformed devices that already contained a permanent conducting filament. This clearly is only remotely relevant to the discussion of the electroformation process presented here. As noted in the introduction, the model presented in the paper and its experimental evidence agrees with the simulation of the *I–V* characteristics reported by Alexandrov et al. The CC-NDR is caused by increase of the conductivity with temperature and electric field. One could, therefore, pose the question if the observations reported here are consistent with what is known about conductivity mechanisms in oxide thin films. The as-deposited oxide films in memristive devices are typically n-type but highly resistive indicating that the Fermi level is located significantly below the conduction band. The mechanisms most frequently identified as responsible for conductivity in such layers are thermionic emission,[30,31] hopping between defects sites,[32] Poole-Frenkel effect,[33,34] or small polaron hopping.[35] All of these mechanisms result in the conductivity increase at higher temperatures and can lead to thermally induced current constriction. At high electric fields, Poole-Frenkel and hopping-based models could lead to sudden mobility increase by transfer of electrons from localized states to extended band states with high mobility.

6. Conclusion

We argue that electronic current localization precedes permanent filament formation during electroformation in oxide-based resistive switches. The presence of negative differential resistivity in the material causes the device to go into a negative differential resistance regime which causes current constriction. Unless prevented by the circuit load, this process frequently occurs in the form of an uncontrolled runaway. We support these claims by analysis of the steady-state DC behavior and the dynamics of the instability. Both DC and dynamic measurements indicate the presence of an instability that is reversible and, hence, electronic in nature as distinct from structural. The initiation of the constriction is temperature dependent and higher temperature is shown to cause the point of bifurcation to appear at a lower voltage. Hence, we propose the following mechanism of electroforming – with increasing bias, the device conducts uniformly throughout its area. At a well-defined point depending on source voltage, series resistance, temperature and time, the device enters into the *I–V* range of negative differential resistance which results in the electronic current filamentation. This current filamentation starts off with being thermally induced (due to the thermal non-linearities) before the effects of voltage non-linearity set in. This final stage of current filamentation causes the device to change resistance to a value close to the post-forming value. We estimate the localized temperature in the current filament using a self-consistent electro-thermal measurements and simulation. Temperature excursions that exceed 500 K (over the ambient) were estimated in a localized sub-20 nm region on the onset of forming. This localized temperature excursion then triggers the physical changes in the structure to form the permanent filament. The constriction can be controlled with the use the external circuit loading thus affecting the permanent filament structure.

7. Experimental Section

All measured Ta_2O_{5-x} layers were 60 nm thick whereas TiO_{2-x} layers were 20 nm thick, sandwiched between 5 nm Ti and 15 nm Pt as bottom electrode (BE) and 20 nm Pt as top electrode (TE). The Ta_2O_{5-x} samples were deposited using RF sputtering, at 60 W RF power, at 400 °C. The TiO_{2-x} samples were deposited using oxygen plasma based atomic layer deposition (ALD) at 200 °C. SEM imaging was done using FEI Sirion 600 SEM with a through-lens-detector (TLD). More details about the sample preparation and testing in our previous works on TiO_{2-x} and Ta_2O_{5-x}.[25,40,41]

Supporting Information

Supporting Information is available from the Wiley Online Library or from the author.

Acknowledgements

This work was in supported by the SRC Contract 2012-VJ-2247, the NSF Grant DMR1105291 and AFOSR Grant No. FA95501010365. AAS and JAB are thankful to Jonathan A. Malen and Wee-liat Ong for help with thermal conductivity measurements.

Received: February 10, 2014
Revised: May 11, 2014
Published online: July 9, 2014

[1] R. Waser, M. Aono, *Nature. Mater.* **2007**, *6*, 833.
[2] S. Seo, S. M. J. Lee, D. H. Seo, E. J. Jeoung, D.-S. Suh, Y. S. Joung, I. K. Yoo, I. R. Hwang, S. H. Kim, I. S. Byun, J.-S. Kim, J. S. Choi, B. H. Park, *Appl. Phys. Lett.* **2004**, *85*, 5655.
[3] R. Waser, R. Dittmann, G. Staikov, K. Szot, *Adv. Mater.* **2009**, *21*, 2632.
[4] J. J. Yang, M.-X. Zhang, J. P. Strachan, F. Miao, M. D. Pickett, R. D. Kelley, G. M. Ribeiro, R. S. Williams, *Appl. Phys. Lett.* **2010**, *97*, 232102.
[5] G. I. Meijer, *Science* **2008**, *319*, 1625.
[6] T. Yanagida, K. Nagashima, K. Oka, M. Kanai, A. Klamchuen, B. H. Park, T. Kawai, *Sci. Rep.* **2013**, *3*, 1657.
[7] M. J. Lee, C. B. Lee, D. Lee, S. R. Lee, M. Chang, J. H. Hur, Y.-B. Kim, C.-J. Kim, D. H. Seo, S. Seo, U.-I. Chung, I.-K. Yoo, K. Kim, *Nature Mater.* **2011**, *10*, 625.
[8] J. J. Yang, M. D. Pickett, X. Li, D. A. A. Ohlberg, D. R. Stewart, R. S. Williams, *Nature Nanotechnol.* **2008**, *3*, 429.
[9] J. Y. Son, Y.-H. Shin, *Appl. Phys. Lett.* **2008**, *92*, 222106.
[10] Q. Zhou, Q. Lu, X. Zhang, Y. Song, Y. Y. Lin, X. Wu, *Appl. Surf. Sci.* **2013**, *271*, 407.
[11] D.-H. Kwon, K. M. Kim, J. H. Jang, J. M. Jeon, M. H. Lee, G. H. Kim, C. S. Hwang, *Nature Nanotechnol.* **2010**, *5*, 148.
[12] S. R. Ovshinsky, *Phys. Rev. Lett.* **1968**, *21*, 1450.
[13] D. W. Greve, *IEEE J. Solid-State Circuits* **1982**, *17*, 349.
[14] L. Goux, Y.-Y. Chen, L. Pantisano, X.-P. Wang, G. Groeseneken, M. Jurczak, D. J. Wouters, *Electrochem. Solid-State Lett.* **2010**, *13*, G54.
[15] S. B. Lee, H. K. Yoo, S. H. Chang, L. G. Gao, B. S. Kang, M.-J. Lee, C. J. Kim, T. W. Noh, *Appl. Phys. Lett.* **2011**, *98*, 053503.
[16] A. S. Alexandrov, A. M. Bratkovsky, B. Bridle, S. E. Savel'ev, D. B. Strukov, R. S. Williams, *Appl. Phys. Lett.* **2011**, *99*, 202104.
[17] F. Palumbo, E. Miranda, G. Ghibaudo, V. Jousseaume, *IEEE Electron Dev. Lett.* **2012**, *33*, 1057.
[18] S. B. Lee, H. K. Yoo, K. Kim, J. S. Lee, Y. S. Kim, S. Sinn, D. Lee, B. S. Kang, B. Kahng, T. W. Noh, *Nanotechnology* **2012**, *23*, 315202.
[19] F. De Stefano, M. Houssa, V. V. Afanas'ev, J. A. Kittl, M. Jurczak, A. Stesmans, *Thin Solid Films* **2013**, *533*, 15, 533.
[20] X. Guan, S. Yu, H.-S. P. Wong, *Electron Devices, IEEE Trans.* **2012**, *59*, 1172.
[21] D. C. Kim, S. Seo, S. E. Ahn, D.-S. Suh, M. J. Lee, B.-H. Park, I. K. Yoo, I. G. Baek, H.-J. Kim, E. K. Yim, J. E. Lee, S. O. Park, H. S. Kim, U-In Chung, J. T. Moon, B. I. Ryu, *Appl. Phys. Lett.* **2006**, *88*, 202102.
[22] B. Gao, S. Yu, H. S. P. Wong, 2010 International Symposium on VLSI Technology Systems and Applications (VLSI-TSA), pp.144–145, April **2010**.
[23] Y. M. Lu, W. Jiang, M. Noman, J. A. Bain, P. A. Salvador, M. Skowronski, *J. Phys. D: Appl. Phys.* **2011**, *44*, 185103.
[24] E. Schöll, *Physica Scripta* **1989**, *T29*, 152.
[25] M. Noman, A. A. Sharma, Y. M. Lu, M. Skowronski, P. A. Salvador, J. A. Bain, *Appl. Phys. Lett.* **2013**, *102*, 023507.
[26] J. P. Strachan, M. D. Pickett, J. J. Yang, S. Aloni, A. L. D. Kilcoyne, G. Medeiros-Ribeiro, R. S. Williams, *Adv. Mater.* **2010**, *22*, 3573.
[27] T. W. Hickmott, *J. Appl. Phys.* **1964**, *35*, 2118.
[28] K. L. Chopra, *J. Appl. Phys.* **1965**, *36*, 184.
[29] F. Argall, *Solid State Electronics* **1968**, *11*, 535.
[30] S. Blonkowski, M. Regache, A. Halimaoui, *J. Appl. Phys.* **2001**, *90*, 1501.
[31] W. Zeng, E. Eisenbraun, H. Frisch, J. J. Sullivan, A. E. Kaloyeros, J. Margalit, K. Beck, *J. Electrochem. Soc.* **2004**, *151*, F172.
[32] C. Chaneliere, J. L. Autran, R. A. B. Devine, *J. Appl. Phys.* **1999**, *86*, 480.
[33] W. K. Choi, C. H. Ling, *J. Appl. Phys.* **1994**, *75*, 3987.
[34] R. A. B. Devine, L. Vallier, J. L. Autran, P. Paillet, J. L. Leray, *Appl. Phys. Lett.* **1996**, *68*, 1775.
[35] R. M. Fleming, D. V. Lang, C. D. W. Jones, M. L. Steigerwald, D. W. Murphy, G. B. Alers, Y.-H. Wong, R. B. van Dover, J. R. Kwo, A. M. Sergent, *J. Appl. Phys.* **2000**, *88*, 850.
[36] D. Ielmini, C. Cagli, F. Nardi, *Appl. Phys. Lett* **2009**, *94*, 063511.
[37] J. J. Yang, M. D. Pickett, X. Li, D. A. A. Ohlberg, D. R. Stewart, R. S. Williams, *Nanotechnology* **2009**, *20*, 215201.
[38] R. Waser, R. Dittmann, G. Staikov, K. Szot, *Adv. Mater.* **2009**, *21*, 2632.
[39] G. Bersuker, D. C. Gilmer, D. Veksler, P. Kirsch, L. Vandelli, A. Padovani, L. Larcher, K. McKenna, A. Shluger, V. Iglesias, M. Porti, M. Nafría, *J. Appl. Phys.* **2011**, *110*, 124518.
[40] M. Noman, A. A. Sharma, Y. M. Lu, R. Kamaladasa, M. Skowronski, P. A. Salvador, J. A. Bain, *Appl. Phys. Lett.* **2014**, *104*, 113510.
[41] A. A. Sharma, M. Noman, M. Skowronski, P. A. Salvador, J. A. Bain, Skowronski, P. A. Salvador, J. A. Bain, *IEEE Integrated Reliability Workshop Final Report (IRW)*, **2013**, 146–149.
[42] S. Menzel, M. Waters, A. Marchewka, U. Böttger, R. Dittmann, R. Waser, *Adv. Funct. Mater.* **2011**, *21*, 4487.